

# SCIENTIFIC REPORTS



OPEN

## Single Layer Bismuth Iodide: Computational Exploration of Structural, Electrical, Mechanical and Optical Properties

Received: 12 August 2015  
Accepted: 02 November 2015  
Published: 02 December 2015

Fengxian Ma<sup>1</sup>, Mei Zhou<sup>4</sup>, Yalong Jiao<sup>1</sup>, Guoping Gao<sup>1</sup>, Yuantong Gu<sup>1</sup>, Ante Bilic<sup>2</sup>, Zhongfang Chen<sup>3</sup> & Aijun Du<sup>1</sup>

Layered graphitic materials exhibit new intriguing electronic structure and the search for new types of two-dimensional (2D) monolayer is of importance for the fabrication of next generation miniature electronic and optoelectronic devices. By means of density functional theory (DFT) computations, we investigated in detail the structural, electronic, mechanical and optical properties of the single-layer bismuth iodide (BiI<sub>3</sub>) nanosheet. Monolayer BiI<sub>3</sub> is dynamically stable as confirmed by the computed phonon spectrum. The cleavage energy ( $E_d$ ) and interlayer coupling strength of bulk BiI<sub>3</sub> are comparable to the experimental values of graphite, which indicates that the exfoliation of BiI<sub>3</sub> is highly feasible. The obtained stress-strain curve shows that the BiI<sub>3</sub> nanosheet is a brittle material with a breaking strain of 13%. The BiI<sub>3</sub> monolayer has an indirect band gap of 1.57 eV with spin orbit coupling (SOC), indicating its potential application for solar cells. Furthermore, the band gap of BiI<sub>3</sub> monolayer can be modulated by biaxial strain. Most interestingly, interfacing electrically active graphene with monolayer BiI<sub>3</sub> nanosheet leads to enhanced light absorption compared to that in pure monolayer BiI<sub>3</sub> nanosheet, highlighting its great potential applications in photonics and photovoltaic solar cells.

Since the discovery of graphene and its excellent electronic/mechanical properties<sup>1,2</sup>, tremendous research efforts have been focusing on searching new two-dimensional (2D) materials such as hexagonal boron nitride, transition metal dichalcogenides, and transition metal halides<sup>3-9</sup>. These 2D materials are bringing revolutions to numerous advanced applications due to their unique and fascinating physical and chemical properties. For example, monolayer MoS<sub>2</sub> can be used as transistors with room-temperature current on/off ratios of 10<sup>8</sup>. The advantages of 2D materials are so appealing that it is strongly desirable to explore a wide range of 2D materials, other than graphene, to satisfy different purposes. For example, 2D materials with a suitable band gap would meet the needs of field effect transistors or optoelectronic devices<sup>10-12</sup>. More interestingly, a new family of 2D materials, i.e., van der Waals type hetero-structures, can be assembled in a designed manner, which has already proven successful for a number of electronic applications in the area of ultrathin and flexible devices<sup>13-17</sup>. Over the past decade, a number of experimental methods have been developed to exfoliate layered materials in order to produce monolayer nanosheets, such as liquid exfoliation that involves oxidation, ion intercalation/exchange, or surface passivation by solvents<sup>18,19</sup>.

<sup>1</sup>School of Chemistry, Physics and Mechanical Engineering, Science and Engineering Faculty, Queensland University of Technology (QUT), Gardens Point Campus, QLD 4001, Brisbane, Australia. <sup>2</sup>CSIRO Manufacturing, Virtual Nanoscience Lab, Parkville 3052 VIC, Australia. <sup>3</sup>Department of Chemistry, Institute for Functional Materials, University of Puerto Rico, San Juan, PR 00931, United States. <sup>4</sup>Department of Physics and State Key Laboratory of Low-Dimensional Quantum Physics, Tsinghua University, Beijing 100084, People's Republic of China. Correspondence and requests for materials should be addressed to A.D. (email: aijun.du@qut.edu.au)

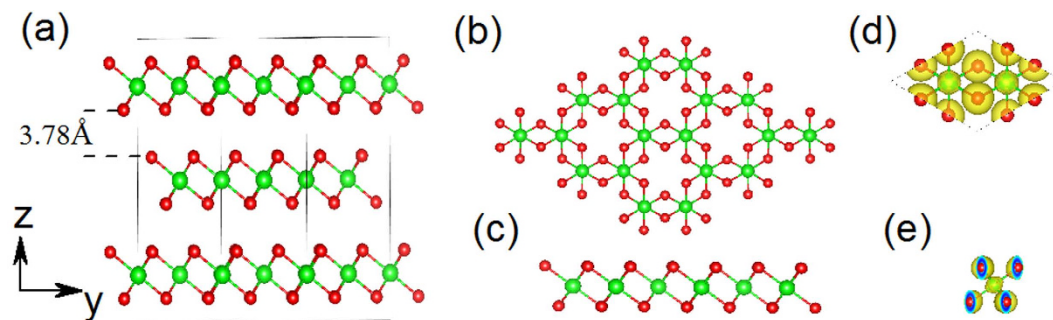


**Figure 1.** (a) Side view of  $\text{BiI}_3$  bulk crystal; (b) top and (c) side views of  $\text{BiI}_3$  nanosheet; red and green ball represent the iodine and bismuth atoms, respectively; (d) top and (e) side views of Iso-surface ( $0.045 \text{ eV}/\text{au}^3$ ) for electronic density of monolayer  $\text{BiI}_3$ .

Some theoretical methods have been developed and employed to search new quasi-two-dimensional (Q2D) materials such as particle swarm optimization (PSO), “atom substitution” and “mechanical exfoliation”. PSO is generally used to locate the global minimum structure. Using PSO, Li *et al.* discovered a novel 2D inorganic material, namely  $\text{Be}_2\text{C}$  monolayer, in which each carbon atom binds to six Be atoms in an almost planar fashion, forming a quasi-planar hexa-coordinate carbon moiety<sup>20</sup>; Tan *et al.* predicted that the  $\text{BSi}_3$  silicene containing planar cyclic six-membered silicon rings (c- $\text{BSi}_3$ ) is the global minimum of  $\text{BSi}_3$  monolayer<sup>21</sup>. Additionally, atom substitution to the common layered structure is used to construct other new types of 2D materials. For instance, by atom substitution of the considered single layer structure, Arunima *et al.* examined the structure, stability, and electronic properties of 2D material in the family of group-IV mono-chalcogenides<sup>22</sup>. “Mechanical exfoliation” is applied to obtain monolayer directly from their layered bulk structures. Zhao *et al.* predicted that the freestanding  $\text{Ca}_2\text{N}$  monolayer could be exfoliated from the bulk, and therefore obtaining 2D electron gas in free space without resorting to electron doping<sup>13</sup>.

Up to now, a diverse range of intriguing properties in 2D materials have been revealed, highlighting the potential use for important applications in energy<sup>23</sup>, photonics<sup>10,24,25</sup> and nanoelectronics<sup>26–28</sup>. However, the practical applications based on 2D materials are still very limited, because they suffer from serious bandgap hurdles, e.g. the lack of obvious gap in graphene<sup>29</sup> and too large gap in boron nitride<sup>30</sup>. Single-layer transition metal dichalcogenides such as  $\text{MoS}_2$  possess an appropriate bandgap<sup>31</sup>, but are strongly influenced by metal contacts, interface traps, charged impurities, dielectric environment, and structural defects<sup>32–34</sup>. Therefore, the search for new types of 2D structures is of paramount importance for the fabrication of next generation nanodevices.

Bismuth tri-iodide ( $\text{BiI}_3$ ) is a typical metal halide, the stacking in bulk counterpart is in ABC order with highly ionic Bi-I bond within the layers and weak van der Waals interaction between layers (Fig. 1a). It has been used for room temperature gamma-ray detection, primarily due to its intermediate band gap, high density, and high effective atomic number<sup>35,36</sup>. The structural, electronic and optical properties of  $\text{BiI}_3$  crystal have been reported both experimentally and theoretically<sup>37–39</sup>. Podraza *et al.* demonstrated the strong spin-orbital coupling (SOC) effect in bulk  $\text{BiI}_3$ <sup>40</sup>. Meanwhile, the  $\text{BiI}_3$  thin films and plates have been synthesized by different approaches such as thermal evaporation<sup>41</sup>, hot wall technique<sup>42,43</sup> and physical vapour deposition<sup>35</sup>. Exploring the  $\text{BiI}_3$  nanostructures is beneficial to gain insights into the properties of  $\text{BiI}_3$  at the atomic scale. So far, single-layer  $\text{BiI}_3$  nanosheet has not been synthesized. Under this context, a systematic theoretical investigation on its structure, stability, electronic, mechanical and optical properties can not only enhance our understanding to their intrinsic characteristics, but also provide useful guidelines for the experimental synthesis of monolayer  $\text{BiI}_3$  and facilitate their practical applications.

In this work, by means of density functional theory (DFT) computations, we first evaluate the stability of monolayer  $\text{BiI}_3$  and the feasibility to exfoliate it from the bulk phase. Subsequently the electronic, mechanical and optical properties of monolayer  $\text{BiI}_3$  nanosheets are investigated. We find that the SOC is significant and can reduce bandgap by around 1.0 eV in monolayer  $\text{BiI}_3$  nanosheet. In addition, the band gap can be modulated with a biaxial strain. Most interestingly, forming a 2D van der Waals type heterostructure by interfacing electrically active graphene with single-layer  $\text{BiI}_3$  nanosheet can significantly enhance the visible light response, i.e., shifting the absorption edge by 2 eV for a hybrid graphene/ $\text{BiI}_3$  nanocomposite compared to that for a pure single  $\text{BiI}_3$  nanosheet, which suggests its potential applications in optoelectronics and photovoltaics.

### Computational details

All the calculations were performed employing the generalized gradient approximation in the Perdew-Burke-Ernzerhof form (GGA-PBE)<sup>44</sup> and the projector augmented wave method<sup>45,46</sup>, as implemented in Vienna *ab initio* simulation package (VASP)<sup>47,48</sup>. A dispersion correction of the total energy (DFT-D3 method)<sup>49</sup>

was used to simulate the long-range van der Waals interaction. The plane-wave energy cutoff was set to 400 eV for geometry optimization and to 500 for static electronic structure and optical property computations. To study 2D systems under the periodic boundary conditions, a vacuum layer with a thickness of at least 20 Å is inserted to avoid the interaction between periodic images. All the geometry structures were fully relaxed until energy and force were converged to  $1\text{E}^{-5}\text{eV}$  and  $0.005\text{eV}/\text{Å}$ , respectively. Unit cell of  $\text{BiI}_3$  (containing 8 atoms) with  $5 \times 5 \times 1$ ,  $9 \times 9 \times 1$  and  $17 \times 17 \times 1$  Monkhorst–Pack k-point sampling were used for  $\text{BiI}_3$  monolayer geometry optimization, static electronic structure and optical property calculations, respectively. Phonon dispersion analysis was performed using the Phonopy code<sup>50</sup> interfaced with the density functional perturbation theory<sup>51</sup> implemented in VASP. In phonon calculations, an increased plane wave energy cutoff of 500 eV and an  $11 \times 11 \times 1$  k-point sampling were employed, accompanying with more stringent convergence criteria.

The hybrid graphene/ $\text{BiI}_3$  nanocomposite was simulated using a  $1 \times 1$  unit cell for  $\text{BiI}_3$  which matches well with the  $3 \times 3$  supercell of graphene. The corresponding lattice mismatch is about 2%. In nanocomposite calculations, the k-point mesh used for geometry optimization and static calculation was  $5 \times 5$  and  $15 \times 15$ , respectively.

The frequency-dependent dielectric matrix was calculated for the  $\text{BiI}_3$  nanosheet and for the hybrid graphene/ $\text{BiI}_3$  nanocomposite. The imaginary part is determined by a summation over empty states using the equation<sup>52</sup>:

$$\varepsilon''_{\alpha\beta}(\omega) = \frac{4\pi^2 e^2}{\Omega} \lim_{q \rightarrow 0} \frac{1}{q^2} \sum_{c,v,k} 2\omega_k \delta(\varepsilon_{ck} - \varepsilon_{vk} - \omega) \times \langle \mu_{ck+e_{\alpha q}} | \mu_{vk} \rangle \langle \mu_{ck+e_{\alpha q}} | \mu_{vk} \rangle^* \quad (1)$$

where the indices  $c$  and  $v$  represent conduction and valence band states, respectively.  $\mu_{ck}$  refers to the cell periodic part of the orbitals at the k-point. A large number of empty (conduction band) states are included for the summation in the equation.

## Results and Discussion

**Structure of bulk and monolayer  $\text{BiI}_3$ .** The stacking order in a bulk Bismuth tri-iodide ( $\text{BiI}_3$ ) is ABC with highly ionic Bi-I bond within the layers and weak van der Waals interaction between layers as shown in Fig. 1(a). The interlayer distance is 3.38 Å in the bulk  $\text{BiI}_3$ . For single layer  $\text{BiI}_3$  (Fig. 1(b,c)), bismuth atom planes are located between top and bottom iodide atomic planes, which forms the sequence I–Bi–I plane. The bond length between bismuth and iodine atom is about 3.1 Å, which is similar to that in the bulk  $\text{BiI}_3$ . The charge density distribution, as shown in Fig. 1(d,e), present the ionic Bi-I bond character in the monolayer  $\text{BiI}_3$ .

**Stabilities and feasibility to realize in experiment.** Before the detailed electronic structure investigations, we firstly examine the dynamic stability of monolayer  $\text{BiI}_3$  nanosheet by calculating its phonon band structure along the high symmetry line from M to  $\Gamma$  to K to M (Fig. 2(a)). Clearly, no imaginary frequency appears in the whole 2D reciprocal space, which confirms the dynamic stability of the  $\text{BiI}_3$  monolayer.

Subsequently, we evaluate the atom binding energy ( $E_b$ ), which is defined as  $E_b = [2E(\text{Bi}) + 6E(\text{I}) - E(\text{BiI}_3)]/8$ , where  $E(\text{Bi})$ ,  $E(\text{I})$ , and  $E(\text{BiI}_3)$  are the total energies of bismuth atom, iodine atom, and  $\text{BiI}_3$  sheet, respectively. Based on this definition, systems with stronger binding strength have larger (positive)  $E_b$  values. The positive binding energy (2.69 eV per atom) indicates that  $\text{BiI}_3$  monolayer is stable.

We then check the possibility to obtain  $\text{BiI}_3$  monolayer via a mechanical exfoliation strategy. Thermodynamically, the exfoliation process should overcome a cleavage energy  $E_{cb}$ , which is determined by the interlayer coupling strength<sup>53</sup>. We simulated the separation of a  $\text{BiI}_3$  monolayer from a neighbouring tri-layer (inset of Fig. 2(b)). The corresponding cleavage energy as a function of distance is shown in Fig. 2(b). The cleavage energy of  $\text{BiI}_3$  (0.43 J/m<sup>2</sup>) is comparable to the experimentally estimated  $E_{cl}$  value of graphite (0.37 J/m<sup>2</sup>).<sup>54</sup> By performing a scan on the separation distance  $d$  of the fracture, we obtain the theoretical cleavage strength  $\sigma$ , which is defined as the maximum derivative of  $E_{cl}$  (Fig. 2(b))<sup>55</sup>. The calculated cleavage strength is about 2.8 GPa, which is similar to the value of graphite (2.10 GPa). Since graphene<sup>55</sup> and many other materials<sup>56</sup> can be exfoliated to obtain 2D atomic crystals, we expect that  $\text{BiI}_3$  is also able to be exfoliated by either Scotch tape or atomic force microscopy tip<sup>57</sup>. Notice that, although the exfoliation process discussed here can be routinely used in laboratory, an effective way to produce  $\text{BiI}_3$  monolayer samples in industry is still an interesting goal to pursue.

**Electronic properties.** With the optimized monolayer  $\text{BiI}_3$  and confirmed dynamic stability, we now turn to study the ground-state band structure and density of states (DOS) of  $\text{BiI}_3$  monolayer (as shown in Fig. 3).

For comparison, we first check the band structure of bulk  $\text{BiI}_3$ . The obtained indirect band gap of bulk  $\text{BiI}_3$  is 1.5 eV with SOC, which is consistent with previous first-principles estimation of 1.55 eV and is also in good agreement with the experimentally-measured band gap of 1.67 eV by Podraza *et al.*<sup>40</sup>

Then, we investigate the electronic properties for the monolayer. Monolayer  $\text{BiI}_3$  nanosheet is found to be an indirect semiconductor with a bandgap of 2.54 eV without SOC, which is slightly larger than that in its bulk counterpart (2.50 eV without SOC). When SOC is included, the obtained indirect band

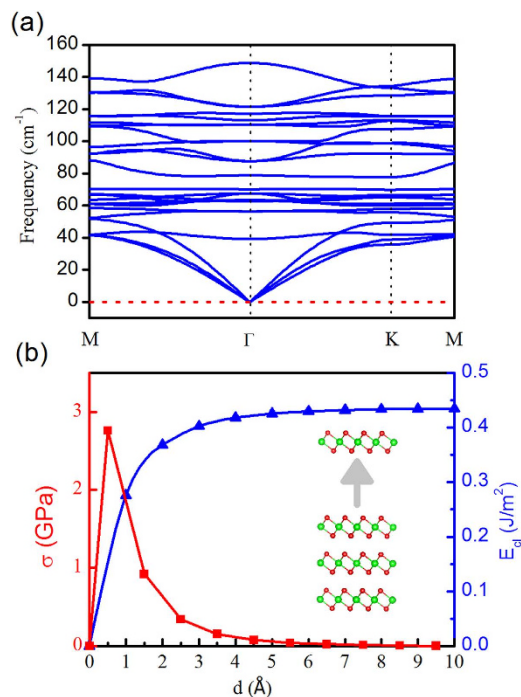


**Figure 2.** (a) Phonon dispersion of BiI<sub>3</sub> monolayer; (b) cleavage energy in J/m<sup>2</sup> (blue line) and its derivative  $\sigma$  in GPa (red line) as a function of the separation distance  $d$  for a fracture in BiI<sub>3</sub> monolayer. Inset: Separating a monolayer from its neighbouring tri-layer.

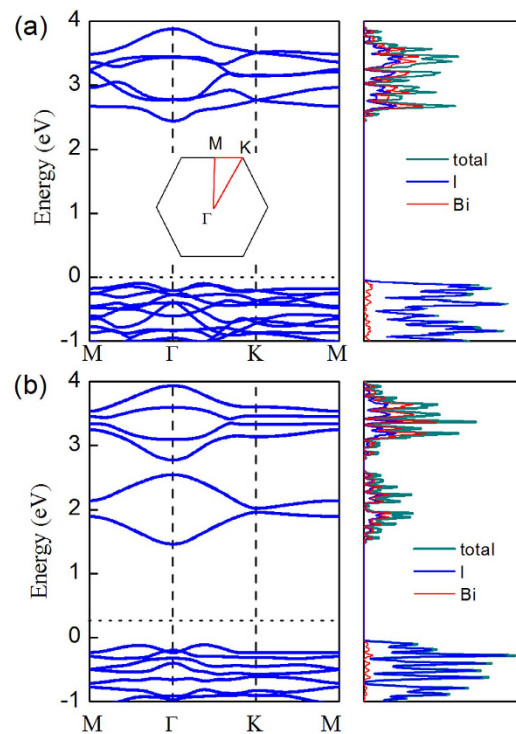


**Figure 3.** Band structure and total DOS of BiI<sub>3</sub> monolayer (a) without SOC; (b) with SOC. Inset is 2D Brillouin zone.

gap for BiI<sub>3</sub> monolayer is reduced to 1.57 eV. The band gap reduction by the PBE-SOC method is mainly attributed to the downward shift of the conducting band edge due to the SOC effect. As we can see from the DOS (right column in the Fig. 3), the valence band maximum (VBM) is mainly composed of I atom,

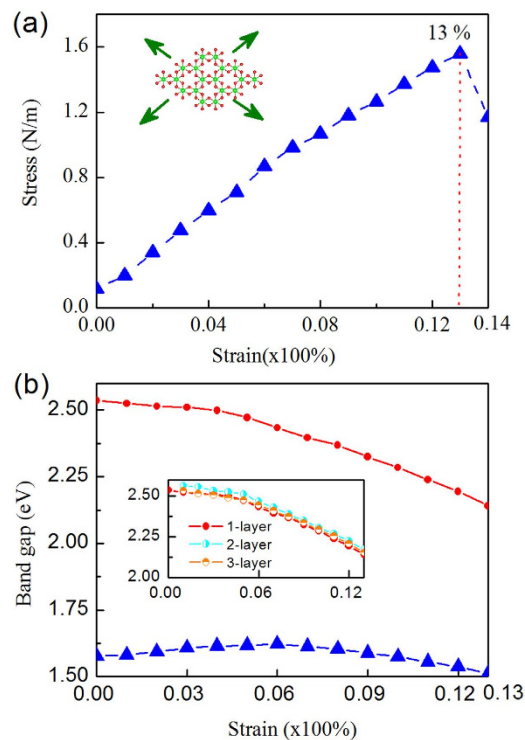


**Figure 4.** (a) Stress-strain curve under biaxial strain. Inset: top view of monolayer BiI<sub>3</sub> and the directions of strain; (b) The band gap at different strain without SOC (red dashed line) and with SOC (blue dashed line); inset: band gap as a function of strain for mono-, bi- and tri- layer BiI<sub>3</sub>.

and the conduction band minimum (CBM) is dominated by the orbitals of Bi atom. Apparently, the SOC effect reduces the energy level in the conducting band for Bi atom.

Therefore, the above results clearly indicate the existence of strong spin orbit effect in monolayer BiI<sub>3</sub>, and the accurate band gap only can be obtained by considering SOC. Note that the band gap of monolayer BiI<sub>3</sub> (1.57 eV by PBE+SOC method) perfectly matches the ideal band gap value of solar cell materials (1.5 eV). Therefore, we expect that monolayer BiI<sub>3</sub> may possess an excellent performance in harvesting the visible light.

**Mechanical properties and the control of electronic properties under mechanical strain.** Knowledge of the mechanical properties of a material provides important information in the selection of suitable applications. A material must have the required properties to function adequately and must be durable enough for the expected product lifetime. Stress-strain curves are an extremely important graphical measure of a material's mechanical properties, which provide a preliminary overview of geometrical change during loading testing. In our computations, the strain is added through the change of lattice parameters, the lattice constant  $a$  of the strained phase is determined by the percentage strain  $h$  ( $a = a_0(1 + h)$ ), where  $a_0$  is the equilibrium lattice constants at 0% at strain. The  $h$  values are from 0 to 14% with an interval of 0.8%. To eliminate the artificial effect of the out-of-plane thickness of the simulation box on the stress, we use the second Piola–Kirchhoff stress<sup>58</sup> to express the 2D forces per length with units of Nm<sup>-1</sup>. The changes of force in various strains indicate the stress–strain relationship.

Figure 4(a) presents the calculated stress-strain curve of BiI<sub>3</sub> monolayer under a biaxial tensile strain. Apparently, the relationship between the stress and strain is linear. The ultimate and breaking strength are at the same point, indicating that the BiI<sub>3</sub> monolayer is a type of brittle material. The ideal strength for the fracture of the BiI<sub>3</sub> monolayer is around 13%.

It is known that strain has remarkable effects in tailoring electronic, optical and transport properties of 2D semiconductors. Experimentally, the external strain can be applied to 2D materials by various techniques, for example by the mismatch of lattice constant and thermal expansion between the substrate and the film. Kim et al. have shown the possibility of applying nearly 30% strain to graphene by the use of stretchable substrates<sup>59</sup>. Therefore a full analysis of the strain effect on the band gap and electronic structure of single layer BiI<sub>3</sub> is highly desired.

Figure 4(b) shows the band gap as a function of the biaxial strain, in which the band gap has a downward trend with increasing tensile strain, regardless the SOC is considered or not. Note that the BiI<sub>3</sub> sheet breaks up at 13%, thus we only study the strain up to this breaking point. With SOC, the change trend of band gap under different strains is moderate, the band gap keeps at 1.57–1.6 eV when the strain

	Monolayer	Bilayer	Tri-layer	Bulk
$E_b$	2.69	2.73	2.74	2.76
a or b	7.64	7.60	7.59	7.54

**Table 1.** The calculated binding energies per atom ( $E_b$ , in eV) and equilibrium lattice constants ( $a$  or  $b$ , in Å) of BiI<sub>3</sub> monolayer, 2-layer, 3-layer and bulk.

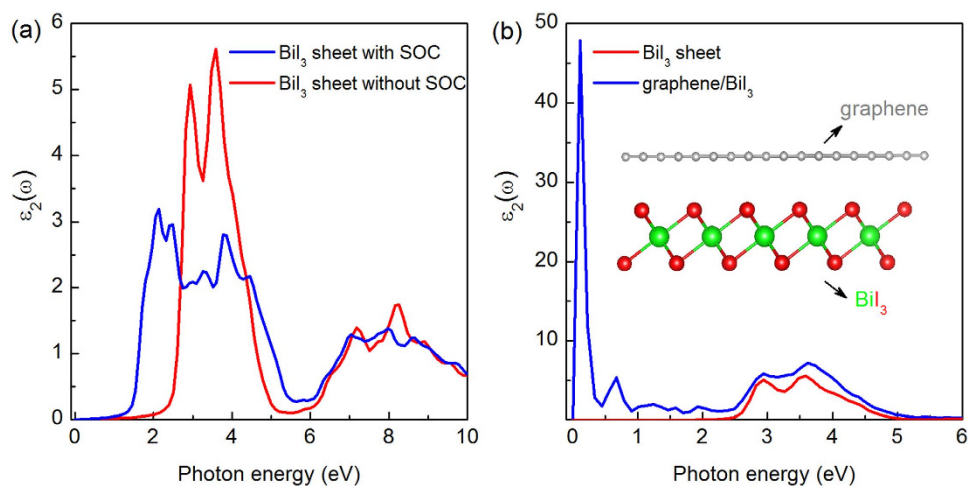


**Figure 5.** (a) The imaginary part of dielectric function  $\varepsilon_2(\omega)$  of BiI<sub>3</sub> monolayer without SOC (red line) and with SOC (blue line); (b)  $\varepsilon_2(\omega)$  of BiI<sub>3</sub> monolayer (red line) and the graphene/BiI<sub>3</sub> composite (blue line).

is less than 6%, then gradually decreases to 1.5 eV at 13%. Without SOC, the gap slowly decreases from 2.54 eV at 0% to 2.45 eV at 5%, then sharply declines to 2.15 eV at 13%. The detailed band structures of BiI<sub>3</sub> under different strains are shown in Supporting Information Fig. S1.

Generally, the properties of 2D nanomaterials are dependent on the thickness. Therefore, we evaluated the effect of thickness on the structure and bandgap-strain relationship. In terms of structure parameters and energy (Table 1), the equilibrium lattice constants are gradually reduced from 7.64 Å in monolayer to 7.60 Å in bilayer and then to 7.59 Å in tri-layer. The binding energy per atom ( $E_b$ ) increases from 2.69 eV of monolayer to 2.73 eV of bilayer then to 2.74 eV of tri-layer, which is consistent with favourable inter-layer binding energies. The lattice length and binding energy of tri-layer (the thickest layer we studied) are still slightly different with those (7.54 Å and 2.76 eV) of bulk. Considering the demanding computational costs for systems with large thickness, we only evaluated the band gap of strained few-layer BiI<sub>3</sub> sheets (2 and 3 layers) without SOC to examine the thickness effect. Our DFT computations showed that the band gaps of 2- and 3- layers decrease with the increase of strain (inserted figure in Fig. 4(b)), which is similar with that for monolayer BiI<sub>3</sub>. This indicates the downward trend is irrelevant to the thickness and the interlayer interaction is indeed rather weak. Therefore, BiI<sub>3</sub> bulk crystals would be an ideal platform to probe 2D electronic property, circumventing the challenge of preparing large-area, single-crystal monolayers.

**Optical properties of BiI<sub>3</sub> nanosheet and the graphene/BiI<sub>3</sub> vdW hetero-structure.** The investigation of optical properties can effectively evaluate the performance of a material in light harvesting, which would therefore benefit our exploration of their potential applications in photovoltaics. In the following we calculate the imaginary part of the dielectric function  $\varepsilon_2(\omega)$  of pure BiI<sub>3</sub> sheet with SOC and without SOC as shown in the Fig. 5(a). When considering SOC, the first peak of  $\varepsilon_2(\omega)$  is in between 1.5 and 2.0 eV, which is in agreement with the value (1.57 eV) of the SOC band gap in Fig. 3(b). Similarly, the first peak from the calculation without SOC, located between 2.5 and 3.0 eV, is consistent with the uncorrected band gap shown in Fig. 3(a). The calculated imaginary part of the dielectric functions of BiI<sub>3</sub> monolayer with SOC shows a red shift about 1.0 eV of absorption edge compared to that without SOC, which indicates the strong effect of SOC to the optical properties of BiI<sub>3</sub> nanosheet.

Recent experiments have shown that a new family of 2D van der Waals type complex based on the combination of highly conductive graphene and optically active MoS<sub>2</sub> can generate photon-excited electron-hole pairs within the band gap of MoS<sub>2</sub>, allowing to achieve enhanced photocurrent in visible light region<sup>60,61</sup>. To explore this effect, we investigated the geometric structure and optical properties of graphene/BiI<sub>3</sub> vdW hetero-structure (G/BiI<sub>3</sub>) without SOC effect because it is difficult to include SOC

for the large system. For the geometry of the hybrid structure, the graphene covered on BiI<sub>3</sub> monolayer (insert figure in Fig. 5(b)), has a binding energy of 0.023 eV per atom with an equilibrium interlayer spacing of about 3.67 Å. Therefore, interaction between graphene and the BiI<sub>3</sub> monolayer is very weak, a typical van der Waals interaction.

As shown in Fig. 5(b), the calculated imaginary part of the dielectric functions of hybrid G/BiI<sub>3</sub> displays an abrupt peak at 0.1 eV, which demonstrates the red shift of absorption edge is as large as 2.0 eV compared to that for the pristine BiI<sub>3</sub> nanosheet. The peak at 0.1 eV also indicates the remarkable enhanced abilities to absorb low-energy photons. Furthermore, the hybrid G/BiI<sub>3</sub> absorbs more photons in visible light region (1.5–3.0 eV) because of the higher  $\epsilon_2(\omega)$ . Therefore, the hybrid G/BiI<sub>3</sub> nano-composite is expected to display enhanced photo-catalytic activities under sunlight irradiation.

## Conclusions

In summary, we theoretically investigated the stability, electronic, mechanical and optical properties of BiI<sub>3</sub> nanosheet by means of DFT computations. BiI<sub>3</sub> monolayer is dynamically stable, and it is rather feasible to exfoliate the monolayer from the bulk. The BiI<sub>3</sub> nanosheet is a brittle material with a breaking strain of 13%. The SOC effect is important to compute the band structure of BiI<sub>3</sub> nanosheet, and the 1.57 eV band gap (with the inclusion of SOC) matches the ideal band gap value of solar cell materials. Moreover, the band gap of BiI<sub>3</sub> monolayer is strain controllable, and the BiI<sub>3</sub> films are insensitive to the thickness. Most interestingly, interfacing electrically active graphene with monolayer BiI<sub>3</sub> nanosheet shows enhanced light absorption compared to that in the pristine monolayer BiI<sub>3</sub> nanosheet. All these unique and exception properties endow BiI<sub>3</sub> nanosheet and its composites great potentials for photonics and photovoltaic solar cells.

## References

1. Avouris, P. Graphene: Electronic and Photonic Properties and Devices. *Nano Lett.* **10**, 4285–4294, doi: 10.1021/nl102824h (2010).
2. Cao, G. Atomistic Studies of Mechanical Properties of Graphene. *Polymers* **6**, 2404–2432, doi: 10.3390/polym6092404 (2014).
3. Nicolosi, V., Chhowalla, M., Kanatzidis, M. G., Strano, M. S. & Coleman, J. N. Liquid Exfoliation of Layered Materials. *Science* **340**, doi: 10.1126/science.1226419 (2013).
4. Tang, Q. & Zhou, Z. Graphene-analogous low-dimensional materials. *Prog. Mater. Sci.* **58**, 1244–1315, doi: 10.1016/j.pmatsci.2013.04.003 (2013).
5. Miro, P., Audiffred, M. & Heine, T. An atlas of two-dimensional materials. *Chem. Soc. Rev.* **43**, 6537–6554, doi: 10.1039/C4CS00102H (2014).
6. Xu, M., Liang, T., Shi, M. & Chen, H. Graphene-Like Two-Dimensional Materials. *Chem. Rev.* **113**, 3766–3798, doi: 10.1021/cr300263a (2013).
7. Lin, S.-H. & Kuo, J.-L. Towards the ionic limit of two-dimensional materials: monolayer alkaline earth and transition metal halides. *PCCP* **16**, 20763–20771, doi: 10.1039/C4CP02048K (2014).
8. Geim, A. K. & Grigorieva, I. V. Van der Waals heterostructures. *Nature* **499**, 419–425, doi: 10.1038/nature12385 (2013).
9. Tang, Q., Zhou, Z. & Chen, Z. Innovation and discovery of graphene-like materials via density-functional theory computations. *Wiley Interdiscip. Rev. Comput. Mol. Sci.* **5**, 360–379, doi: 10.1002/wcms.1224 (2015).
10. Jiao, Y. *et al.* Versatile Single-Layer Sodium Phosphidostannate(II): Strain-Tunable Electronic Structure, Excellent Mechanical Flexibility, and an Ideal Gap for Photovoltaics. *J. Phys. Chem. Lett.* **6**, 2682–2687, doi: 10.1021/acs.jpcllett.5b01136 (2015).
11. Tang, Q., Zhou, Z., Shen, P. & Chen, Z. Band Gap Engineering of BN Sheets by Interlayer Dihydrogen Bonding and Electric Field Control. *ChemPhysChem* **14**, 1787–1792, doi: 10.1002/cphc.201300141 (2013).
12. Tang, Q., Bao, J., Li, Y., Zhou, Z. & Chen, Z. Tuning band gaps of BN nanosheets and nanoribbons via interfacial dihalogen bonding and external electric field. *Nanoscale* **6**, 8624–8634, doi: 10.1039/C4NR00008K (2014).
13. Zhao, S., Li, Z. & Yang, J. Obtaining two-dimensional electron gas in free space without resorting to electron doping: an electronegative based design. *J. Am. Chem. Soc.* **136**, 13313–13318, doi: 10.1021/ja5065125 (2014).
14. Du, A. & Smith, S. C. Electronic Functionality in Graphene-Based Nanoarchitectures: Discovery and Design via First-Principles Modeling. *J. Phys. Chem. Lett.* **2**, 73–80, doi: 10.1021/jz101347a (2011).
15. Britnell, L. *et al.* Strong Light-Matter Interactions in Heterostructures of Atomically Thin Films. *Science* **340**, 1311–1314, doi: 10.1126/science.1235547 (2013).
16. Du, A. *et al.* Hybrid Graphene/Titania Nanocomposite: Interface Charge Transfer, Hole Doping, and Sensitization for Visible Light Response. *J. Phys. Chem. Lett.* **2**, 894–899, doi: 10.1021/jz2002698 (2011).
17. Jiao, Y. *et al.* Graphene-covered perovskites: an effective strategy to enhance light absorption and resist moisture degradation. *RSC Adv.* **5**, 82346–82350, doi: 10.1039/C5RA14381K (2015).
18. Valeria Nicolosi, 2 Manish Chhowalla, 3 Mercouri G. Kanatzidis, 4 & Michael S. Strano, J. N. C. Liquid Exfoliation of Layered Materials. *Science* **334**, 72–75, doi: 10.1126/science.1208891 (2013).
19. Paton, K. R. *et al.* Scalable production of large quantities of defect-free few-layer graphene by shear exfoliation in liquids. *Nat Mater* **13**, 624–630, doi: 10.1038/nmat3944 (2014).
20. Li, Y., Liao, Y. & Chen, Z. Be<sub>2</sub>C Monolayer with Quasi-Planar Hexacoordinate Carbons: A Global Minimum Structure. *Angew. Chem. Int. Ed.* **53**, 7248–7252, doi: 10.1002/anie.201403833 (2014).
21. Tan, X., Li, F. & Chen, Z. Metallic BSi<sub>3</sub> Silicene and Its One-Dimensional Derivatives: Unusual Nanomaterials with Planar Aromatic D<sub>6h</sub> Six-Membered Silicon Rings. *J. Phys. Chem. C* **118**, 25825–25835, doi: 10.1021/jp507011p (2014).
22. Singh, A. K. & Hennig, R. G. Computational prediction of two-dimensional group-IV mono-chalcogenides. *Appl. Phys. Lett.* **105**, 042103, doi: 10.1063/1.4891230 (2014).
23. Jing, Y., Zhou, Z., Cabrera, C. R. & Chen, Z. Graphene, inorganic graphene analogs and their composites for lithium ion batteries. *J. Mater. Chem. A* **2**, 12104–12122, doi: 10.1039/C4TA01033G (2014).
24. Tan, X., Cabrera, C. R. & Chen, Z. Metallic BSi<sub>3</sub> Silicene: A Promising High Capacity Anode Material for Lithium-Ion Batteries. *J. Phys. Chem. C* **118**, 25836–25843, doi: 10.1021/jp503597n (2014).
25. Jing, Y., Zhou, Z., Cabrera, C. R. & Chen, Z. Metallic VS<sub>2</sub> Monolayer: A Promising 2D Anode Material for Lithium Ion Batteries. *J. Phys. Chem. C* **117**, 25409–25413, doi: 10.1021/jp410969u (2013).
26. Zhang, S., Yan, Z., Li, Y., Chen, Z. & Zeng, H. Atomically Thin Arsenene and Antimonene: Semimetal–Semiconductor and Indirect–Direct Band-Gap Transitions. *Angew. Chem. Int. Ed.* **54**, 3112–3115, doi: 10.1002/anie.201411246 (2015).

27. Kou, L. *et al.* Structural and Electronic Properties of Layered Arsenic and Antimony Arsenide. *J. Phys. Chem. C* **119**, 6918–6922, doi: 10.1021/acs.jpcc.5b02096 (2015).
28. Zhou, M., Duan, W., Chen, Y. & Du, A. Single layer lead iodide: computational exploration of structural, electronic and optical properties, strain induced band modulation and the role of spin-orbital-coupling. *Nanoscale* **7**, 15168–15174, doi: 10.1039/C5NR04431F (2015).
29. Zhou, S. Y. *et al.* Substrate-induced bandgap opening in epitaxial graphene. *Nat. Mater.* **6**, 770–775, doi: 10.1038/nmat2003 (2007).
30. Tang, Q., Zhou, Z. & Chen, Z. Molecular Charge Transfer: A Simple and Effective Route To Engineer the Band Structures of BN Nanosheets and Nanoribbons. *J. Phys. Chem. C* **115**, 18531–18537, doi: 10.1021/jp2067205 (2011).
31. Wang, Q. H., Kalantar-Zadeh, K., Kis, A., Coleman, J. N. & Strano, M. S. Electronics and optoelectronics of two-dimensional transition metal dichalcogenides. *Nat Nanotechnol* **7**, 699–712, doi: 10.1038/nnano.2012.193 (2012).
32. Feng, L.-p., Su, J. & Liu, Z.-t. Effect of vacancies in monolayer MoS<sub>2</sub> on electronic properties of Mo-MoS<sub>2</sub> contacts. *RSC Adv.* **5**, 20538–20544, doi: 10.1039/C4RA15218B (2015).
33. Kou, L., Du, A., Chen, C. & Frauenheim, T. Strain engineering of selective chemical adsorption on monolayer MoS<sub>2</sub>. *Nanoscale* **6**, 5156–5161, doi: 10.1039/C3NR06670C (2014).
34. Liu, Q. *et al.* Tuning Electronic Structure of Bilayer MoS<sub>2</sub> by Vertical Electric Field: A First-Principles Investigation. *J. Phys. Chem. C* **116**, 21556–21562, doi: 10.1021/jp307124d (2012).
35. Fornaro, L., Cuna, A., Noguera, A., Perez, M. & Mussio, L. Growth of bismuth tri-iodide platelets for room temperature X-ray detection. *Ieee Nucl Sci Conf R* **51**, 3541–3544, doi: 10.1109/Nssmic.2003.1352675 (2004).
36. Matsumoto, M., Hitomi, K., Shoji, T. & Hiratate, Y. Bismuth tri-iodide crystal for nuclear radiation detectors. *IEEE Trans. Nucl. Sci.* **49**, 2517–2520, doi: 10.1109/Tns.2002.803883 (2002).
37. Jellison, G. E., Ramey, J. O. & Boatner, A. A. Optical functions of BiI<sub>3</sub> as measured by generalized ellipsometry. *Phys. Rev. B* **59**, 9718–9721, doi: 10.1103/PhysRevB.59.9718 (1999).
38. Yorikawa, H. & Muramatsu, S. Theoretical study of crystal and electronic structures of BiI<sub>3</sub>. *J. Phys. Condens. Matter.* **20**, 325220, doi: 10.1088/0953-8984/20/32/325220 (2008).
39. Singh, D. J. Structure and optical properties of high light output halide scintillators. *Phys. Rev.* **B82**, doi: 10.1103/PhysRevB.82.155145 (2010).
40. Podraza, N. J. *et al.* Band gap and structure of single crystal BiI<sub>3</sub>: Resolving discrepancies in literature. *J. Appl. Phys.* **114**, 033110, doi: 10.1063/1.4813486 (2013).
41. Garg, A., Tomar, M. & Gupta, V. Synthesis and Characterisation of Thin Films of Bismuth Triiodide for Semiconductor Radiation Detectors. *Conference Papers in Science* 2014, 3, doi: 10.1155/2014/370436 (2014).
42. Shojiro, T., Katsuyosi, W. & Teruo, K. Thin-Film Single-Crystal Growth of BiI<sub>3</sub> by a Hot Wall Technique. *Jpn. J. Appl. Phys.* **29**, 710, doi: 10.1143/JJAP.29.710 (1990).
43. Takeyama, S., Watanabe, K., Ichihara, M., Suzuki, K. & Miura, N. van der Waals epitaxial growth of thin BiI<sub>3</sub> films on PbI<sub>2</sub> and CdI<sub>2</sub> substrates by a hot wall method. *J. Appl. Phys.* **68**, 2735–2738, doi: 10.1063/1.346449 (1990).
44. Perdew, J. P., Burke, K. & Ernzerhof, M. Generalized gradient approximation made simple. *Phys. Rev. Lett.* **77**, 3865–3868, doi: 10.1103/PhysRevLett.77.3865 (1996).
45. Blöchl, P. E. Projector augmented-wave method. *Phys. Rev. B* **50**, 17953–17979, doi: 10.1103/PhysRevB.50.17953 (1994).
46. Kresse, G. & Joubert, D. From ultrasoft pseudopotentials to the projector augmented-wave method. *Phys. Rev. B* **59**, 1758–1775, doi: 10.1103/PhysRevB.59.1758 (1999).
47. Kresse, G. & Furthmüller, J. Efficiency of ab-initio total energy calculations for metals and semiconductors using a plane-wave basis set. *Comput. Mater. Sci.* **6**, 15–50, doi: 10.1016/0927-0256(96)00008-0 (1996).
48. Kresse, G. & Furthmüller, J. Efficient iterative schemes for ab initio total-energy calculations using a plane-wave basis set. *Phys. Rev. B* **54**, 11169–11186, doi: 10.1103/PhysRevB.54.11169 (1996).
49. Grimme, S. Semiempirical GGA-type density functional constructed with a long-range dispersion correction. *J. Comput. Chem.* **27**, 1787–1799, doi: 10.1002/jcc.20495 (2006).
50. Togo, A., Oba, F. & Tanaka, I. First-principles calculations of the ferroelastic transition between rutile-type and CaCl<sub>2</sub>-type SiO<sub>2</sub> at high pressures. *Phys. Rev. B* **78**, 134106, doi: 10.1103/PhysRevB.78.134106 (2008).
51. Gonze, X. & Lee, C. Dynamical matrices, born effective charges, dielectric permittivity tensors, and interatomic force constants from density-functional perturbation theory. *Phys. Rev. B* **55**, 10355–10368, doi: 10.1103/PhysRevB.55.10355 (1997).
52. Gajdos, M., Hummer, K., Kresse, G., Furthmüller, J. & Bechstedt, F. Linear optical properties in the projector-augmented wave methodology. *Phys. Rev. B* **73**, 045112, doi: 10.1103/PhysRevB.73.045112 (2006).
53. Medvedeva, N. I., Mryasov, O. N., Gornostyrev, Y. N., Novikov, D. L. & Freeman, A. J. First-principles total-energy calculations for planar shear and cleavage decohesion processes in B2-ordered NiAl and FeAl. *Phys. Rev. B* **54**, 13506–13514, doi: 10.1103/PhysRevB.54.13506 (1996).
54. Zacharia, R., Ulbricht, H. & Hertel, T. Interlayer cohesive energy of graphite from thermal desorption of polyaromatic hydrocarbons. *Phys. Rev. B* **69**, 155406, doi: 10.1103/PhysRevB.69.155406 (2004).
55. Novoselov, K. S. *et al.* Electric Field Effect in Atomically Thin Carbon Films. *Science* **306**, 666–669, doi: 10.1126/science.1102896 (2004).
56. Novoselov, K. S. *et al.* Two-dimensional atomic crystals. *Proc. Natl. Acad. Sci. U.S.A.* **102**, 10451–10453, doi: 10.1073/pnas.0502848102 (2005).
57. Hong, S. S. *et al.* Ultrathin Topological Insulator Bi<sub>2</sub>Se<sub>3</sub> Nanoribbons Exfoliated by Atomic Force Microscopy. *Nano Lett.* **10**, 3118–3122, doi: 10.1021/nl101884h (2010).
58. Peng, Q., Ji, W. & De, S. Mechanical properties of the hexagonal boron nitride monolayer: Ab initio study. *Comput. Mater. Sci.* **56**, 11–17, doi: org/10.1016/j.commatsci.2011.12.029 (2012).
59. Kim, K. S. *et al.* Large-scale pattern growth of graphene films for stretchable transparent electrodes. *Nature* **457**, 706–710, doi: 10.1038/nature07719 (2009).
60. Roy, K. *et al.* Graphene-MoS<sub>2</sub> hybrid structures for multifunctional photoresponsive memory devices. *Nat. Nano.* **8**, 826–830, doi: 10.1038/nnano.2013.206 (2013).
61. Yu, L. *et al.* Graphene/MoS<sub>2</sub> Hybrid Technology for Large-Scale Two-Dimensional Electronics. *Nano Lett.* **14**, 3055–3063, doi: 10.1021/nl404795z (2014).

## Acknowledgements

We acknowledge generous grants of high-performance computer time from the computing facility at Queensland University of Technology and Australian National Facility. A.D. greatly appreciates the Australian Research Council QEII Fellowship and financial support of the Australian Research Council under Discovery Project (DP130102420). The first author (F.M.) acknowledges the support through



the CSIRO top-up scholarship. A.B. thanks the CSIRO for support through the Julius Career Award. Z.C. acknowledges the final support by Department of Defense (Grant W911NF-12-1-0083) and NSF (Grant EPS-1002410).

### Author Contributions

F. M. and A. D. conceived the idea. F.M., Y. J. and G. G. performed the calculations. F. M., M. Z., Y. G., A. B., Z. C. and A. D. contributed to the analysis of the results and to the writing of the manuscript.

### Additional Information

**Supplementary information** accompanies this paper at <http://www.nature.com/srep>

**Competing financial interests:** The authors declare no competing financial interests.

**How to cite this article:** Ma, F. *et al.* Single Layer Bismuth Iodide: Computational Exploration of Structural, Electrical, Mechanical and Optical Properties. *Sci. Rep.* **5**, 17558; doi: 10.1038/srep17558 (2015).



This work is licensed under a Creative Commons Attribution 4.0 International License. The images or other third party material in this article are included in the article's Creative Commons license, unless indicated otherwise in the credit line; if the material is not included under the Creative Commons license, users will need to obtain permission from the license holder to reproduce the material. To view a copy of this license, visit <http://creativecommons.org/licenses/by/4.0/>